Microelectronics Reliability 126 (2021) 114209

Contents lists available at ScienceDirect

Microelectronics Reliability

journal homepage: www.elsevier.com/locate/microrel

Constitutive equations for strain rate and temperature dependent mechanical behaviour of porous Ag-sintered joints in electronic packages

M. Lederer [a,b,*], Z. Gökdeniz [a,b], G. Khatibi [a,b], J. Nicolics [b]

[a] Christian Doppler Laboratory for Lifetime and Reliability of Interfaces in Complex Multi-Material Electronics, TU Wien, Getreidemarkt 9, 1060 Vienna, Austria
[b] Institute for Chemical Technologies and Analytics, TU Wien, Getreidemarkt 9, 1060 Vienna, Austria

ARTICLE INFO

Keywords:
Finite element analysis
Creep
Sintered silver

ABSTRACT

Sintering of silver attracts increasing attention in electronic packaging owing to superior bonding quality and high operation temperatures. However, the mechanical properties of sintered joints strongly depend on fabrication parameters like sintering temperature, pressure or organic solvents in the silver paste. In consequence, the mechanical characterization of this material is a challenging task. In the present article, unified constitutive equations for plasticity and creep of sintered silver are established. Thereby, particular interest is devoted to the influence of porosity on the mechanical properties. The assumptions of the model are validated by mechanical tests carried out with samples prepared under constant sintering conditions. The model parameters are fitted to test results performed in tension mode, in shear mode and under conditions of stress relaxation. This material model is implemented in the commercial software ABAQUS through user subroutines UMAT and VUMAT. In conclusion, the constitutive material model can be used as prerequisite for reliability predictions of Ag-sintered joints in electronic packages.

1. Introduction

In the last decade sintering of silver paste at temperatures comparable to those of soldering processes received increasingly attention as novel interconnection technique with particular features like superior bonding properties also at high operation temperatures, the impossibility of formation of quality-degrading intermetallic layers, and the avoidance of flux enclosures [1]. The combination of these features predestine silver sintering as a replacement of soldering for both, embedding and surface attachment of power devices and attracts more and more power electronics manufacturer, since this technique allows double-sided cooling [2], promises a further significant step towards saving weight, reducing package dimensions, parasitic impedances, and cost, while improving ecological measures by avoiding of lead-containing alloys [3]. As consequence of the low sintering temperatures the bonding silver layer exhibits an extremely porous structure which, in turn, is responsible for a conspicuous creep behaviour making it favorable as a highly reliable stress releasing and compliant bonding layer [4,5]. However, since the mechanical properties of this bonding layer strongly depend on fabrication parameters and operation conditions, full use of advantages requires accurate numerical modelling of assemblies during their design phase based on adequate temperature and time dependent material models.

In recent years, several constitutive models were applied to sintered nanosilver. Yu et al. [6] preferred the viscoplastic Anand model [7], because of its temperature and strain rate dependence. Chen et al. [8] also applied the Anand model and compared it to a kinematic hardening model with temperature dependent material parameters. Finite Element simulations showed good agreement between those two models on the one side and experiments on the other. A drawback of the here mentioned models might be that the porosity of sintered silver was not considered in detail. A model including porosity was proposed by Yao and Gong [9]. They started their investigation from the Gurson model [10] and extended it to a model of unified creep and plasticity.

In the present study, a constitutive model is developed from the phenomenological point of view. Mechanical tests were performed in tension, in shear, under cyclic load and under conditions of stress relaxation. Consequently, a constitutive material model is elaborated, which is in accordance with all relevant experiments.

* Corresponding author.
E-mail address: martin.lederer@tuwien.ac.at (M. Lederer).

https://doi.org/10.1016/j.microrel.2021.114209
Received 25 May 2021; Accepted 17 June 2021
Available online 11 October 2021

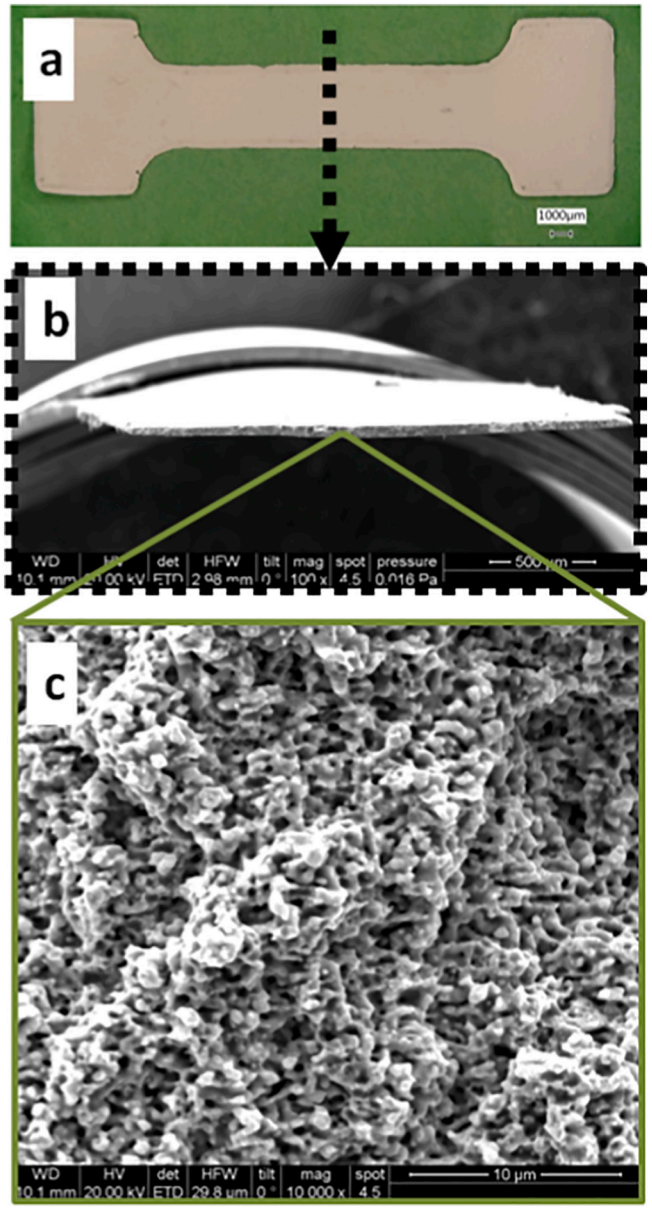

Fig. 1. (a) Dumbbell shaped specimen, (b) and (c) SEM micrographs of its fracture surface.

2. Experimental

Two main types of samples were prepared for mechanical tests. Firstly, dumbbell shaped specimens of sintered silver were produced for uniaxial tensile tests and for stress relaxation after tensile loading. The tests were performed by using a micro tensile machine equipped with a laser speckle extensometer, with load cell capacities of 100 N for the dumbbell shaped samples and 1000 N for the lap-joints. The dumbbell shaped samples had a parallel length of about 30 mm, a width of 4 mm and a thickness of approximately 75 µm. The shape of a sample before testing is depicted in Fig. 1 (a), while Fig. 1 (b) and (c) show the cross section of a tensile sample after rupture.

Secondly, lap-joints connecting two pieces of copper base material with sintered silver were prepared for shear tests under monotonic and cyclic loading, and for testing under conditions of stress relaxation. The pieces of copper base material had a cross section of 3 × 1 mm and a length of 50 mm each. The overlap length of a lap-joint was typically between 4 and 5 mm, and the thickness of the sintered silver layer was in the range between 45 µm and 70 µm, as shown in Fig. 2 (a, c). An EBSD scan of its microstructure is depicted in Fig. 2 (d). Fig. 2 (b) shows a lap-joint sample mounted onto the tensile machine, and the illuminated red dots indicate the position of laser beams of the laser speckle extensometer, which was used for strain measurements.

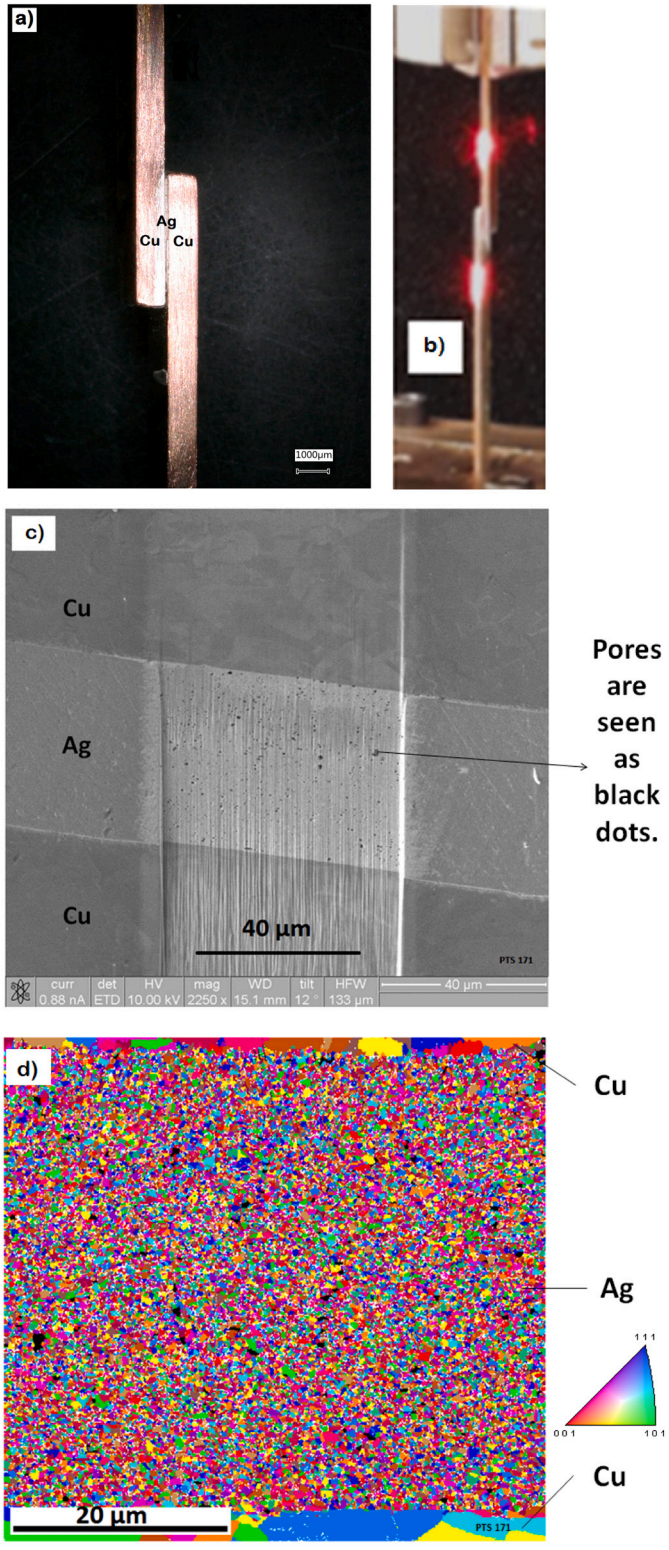

Fig. 2. (a) Cu-Ag-Cu lap-joint, (b) mounted onto a tensile machine, (c) SEM micrograph showing its porosity. (d) EBSD scan showing its grain sizes and orientations.

Table 1
Summary of averaged values for tensile strengths of dumbbell shaped samples and shear strengths of lap-joints.

Test temperature	Dumbbell shaped tensile strength	Lap-joints shear strength
RT	53.2 MPa	33.8 MPa
403 K	42.1 MPa	34 MPa
473 K	42.2 MPa	26.9 MPa

The dumbbell shaped samples and the lap-joints were produced with use of the commercial silver paste Heraeus mAgic 338 under equivalent sintering conditions at a pressure of 70 MPa and a temperature of 503 K, respectively.

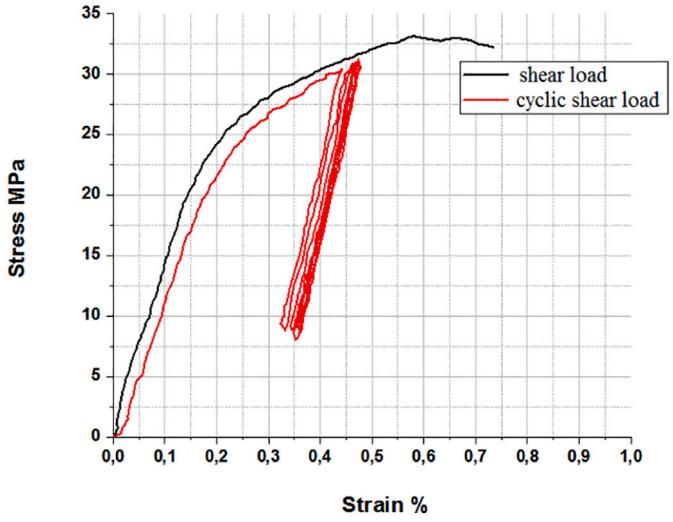

Fig. 3. Stress-strain curves representing the relative longitudinal elongation of a Cu-Ag-Cu lap-joint measured between two points with initial distance of 23 mm.

A metallographic examination confirmed that dumbbell shaped samples and lap-joints showed the same porosity and microstructure. By gravimetric analysis, the porosity was determined as 38%. Further details of the production process used for sintering may be found in references [4,5]. The average tensile and shear strength of the samples at different test temperatures are summarized in Table 1. In stress relaxation experiments, samples were at first loaded to about 75% of their ultimate strength, and thereafter the decay of stress was measured for 1 h. In addition, experiments of cyclic loading and unloading were performed with lap-joints, as shown in Fig. 3.

A collection of cyclic shear experiments with Ag-sintered lap-joints and a detailed description of the setup are included in reference [4].

3. Constitutive model

3.1. Fundamental assumptions

An advanced material model for sintered silver is developed here, whereby meaningful ideas of already existing theories are merged in order to derive optimized accordance with relevant experiments. At first, it is recognized that stress-strain curves of sintered silver under cyclic loading show qualitative agreement with experiments for cyclic loading of metallic fcc bulk material. Such behaviour of cyclic hardening and ratcheting has well been described by a combination of kinematic and isotropic hardening [11]. Therefore, we will take over this method for the present model.

Further, the stress relaxation curves of the present study are in qualitative agreement with experiments of Kariya et al. [12], who fitted this behaviour with the Garofalo model. Moreover, the tensile test data of the present study also show a similarity with experiments, which were successfully interpreted with the Anand model [6,7]. In conclusion, the temperature dependent strain rates are well described by a hyperbolic sine creep law.

Furthermore, it is noticed here that stress relaxation experiments show more compliance under tensile load compared to relaxation under shear load. This behaviour seems to be a consequence of porosity. According to analyses of McClintock [13], Rice and Tracey [14] there occur stress concentrations at the holes of porous metals, which induce plastic deformation and finally lead to rupture. Such stress concentrations increase, when hydrostatic and deviatoric stresses are superimposed. This effect is well described by the Gurson model [10]. In the model of the present study, an orthogonal decomposition of stresses in hydrostatic and deviatoric parts will be utilized to account for this behaviour.

3.2. Constitutive equations

The hydrostatic pressure in a solid is defined as

$$p = -\frac{1}{3} tr(\sigma) \tag{1}$$

where *tr* denotes the trace of a tensor and σ is the Cauchy stress. The deviatoric stress reads as

$$S = \sigma + p \bullet \mathrm{I}, \tag{2}$$

where I is the unity matrix. Further, the volumetric strain is defined as

$$\varepsilon_{vol} = \frac{1}{3} tr(\varepsilon) \bullet \mathrm{I}, \tag{3}$$

while the deviatoric strain writes as

$$\varepsilon_{dev} = \varepsilon - \varepsilon_{vol}. \tag{4}$$

It is assumed that the strain tensor

$$\varepsilon = \varepsilon_{el} + \varepsilon_{ine} \tag{5}$$

can additively be decomposed into an elastic part ε_{el} and an inelastic part ε_{ine}. The accumulated inelastic strain at time t_1 is here defined as

$$\varepsilon_{acc}^{ine} = \int_{t_0}^{t_1} \left\| \dot{\varepsilon}_{ine} \right\| dt, \tag{6}$$

where $\|\varepsilon\|$ denotes the Euklidean norm of the tensor ε. The derivative with respect to time is written according to the dot notation. Next, we define the effective stress

$$\sigma_{eff} = \sigma - \chi \tag{7}$$

where χ is called backstress. The backstress in the material occurs in consequence of the dislocation structure developed during plastic deformation. The backstress follows the time evolution.

$$\dot{\chi} = \chi_0 + k_1 \dot{\varepsilon}_{ine} - k_2 \bullet \varepsilon_{acc}^{ine} \bullet \chi, \tag{8}$$

where k_1 and k_2 are material constants. χ_0 is the initial value of backstress. In context with isotropic hardening, we need to define the deformation resistance

$$D = D_1 \bullet \left(1 - \exp\left\{ -D_2 \bullet \left(\varepsilon_{acc}^{ine} + \varepsilon_0\right) \right\}\right), \tag{9}$$

where D_1 and D_2 are material constants, and ε_0 is the initial value of plastic strain. A value of $\varepsilon_0 > 0$ is needed to obtain a finite value of the deformation resistance in the initial state. Furthermore, a temperature dependent scalar threshold value of

$$\sigma_{th}(T) = A \bullet \left(1 - \exp\left\{ -\frac{Q}{k_B T} \right\}\right) \tag{10}$$

is defined for the stress, below which creep deformation does not occur. Here, Q plays the role of an activation energy, k_B is the Boltzmann constant, $A > 0$ is a material parameter and T is the temperature in units of Kelvin. Thus, we are in the position to define the creep rate of the viscoplastic model. With use of an orthogonal decomposition into volumetric and deviatoric parts, we define the rates of creep strain

$$\left\|\dot{\varepsilon}^{ine}_{vol}\right\| = c_1 \bullet \exp\left\{-\frac{Q}{k_B T}\right\} \bullet \sinh \frac{\left(c_3 \bullet f \bullet \left(\sqrt{3}\,\|p_{eff}\| - \sigma^{vol}_{th}\right)\right)}{D}^{n_1} \tag{11a}$$

$$\left\|\dot{\varepsilon}^{ine}_{dev}\right\| = c_2 \bullet \exp\left\{-\frac{Q}{k_B T}\right\} \bullet \sinh\left(\frac{\|S_{eff}\| - \sigma^{dev}_{th}}{D}\right)^{n_2} \tag{11b}$$

for

$$\left\|\sigma_{eff}\right\| > \sigma_{th} \tag{11c}$$

with

$$\sigma^{vol}_{th} = \frac{\sqrt{3}\left\|p_{eff}\right\|}{\left\|\sigma_{eff}\right\|}\sigma_{th} \tag{11d}$$

and

$$\sigma^{dev}_{th} = \frac{\left\|S_{eff}\right\|}{\left\|\sigma_{eff}\right\|}\sigma_{th}, \tag{11e}$$

where σ^{vol}_{th} and σ^{dev}_{th} are the volumetric and deviatoric parts of the threshold stress. Further, c_1, c_2 and $c_3 > 0$ are material constants and f is the porosity, i.e., the volume fraction of pores in the material. n_1 and n_2 are the stress exponents of the hyperbolic sine creep law. S_{eff} is the deviatoric part of the effective stress σ_{eff}. Due to inelastic volume change in view of porosity, there also occurs a hydrostatic part of the backstress, and in consequence an effective hydrostatic pressure p_{eff}. The volumetric part of strain rate causes compression under positive effective pressure and in the opposite case it leads to expansion. The direction of the deviatoric strain rate is parallel to the effective deviatoric stress S_{eff}. Finally, conservation of mass implies an evolution of porosity according to

$$\dot{f} = (1-f) \bullet \mathrm{tr}\left(\dot{\varepsilon}_{ine}\right) \tag{12}$$

3.3. Damage accumulation

The equations describing the evolution of stresses, strains and porosity of the material are a prerequisite for the formulation of lifetime models. In addition, a rule of damage accumulation is required to obtain reliability assessments based on FEM simulations. In metal plasticity, it is usually assumed that the hydrostatic pressure stress has a small influence on plastic yielding, but a large influence on ductility [13–15]. Under triaxial tension, significant void growth is observed, and this effect appears to be particularly relevant for materials of high porosity. In the case of monotonic loading, the inelastic strain leading to fracture can be described by an equation of the form

$$\varepsilon_f = h_1 \bullet \exp\{-h_2 \bullet p_{eff}\} \tag{13}$$

where h_1 and $h_2 > 0$ are material parameters, while the effective pressure p_{eff} has the same meaning as in Eqs. (11a) and (11d). Further, damage accumulation follows the rule

$$H = \sum \frac{\Delta\varepsilon}{\varepsilon_f}, \tag{14}$$

where H plays the role of a damage variable. Fracture is initiated, when the value of the damage variable H approaches the value of 1. Eqs. (13) and (14) represent a simplified version of a fracture criterion proposed by Johnson and Cook [15].

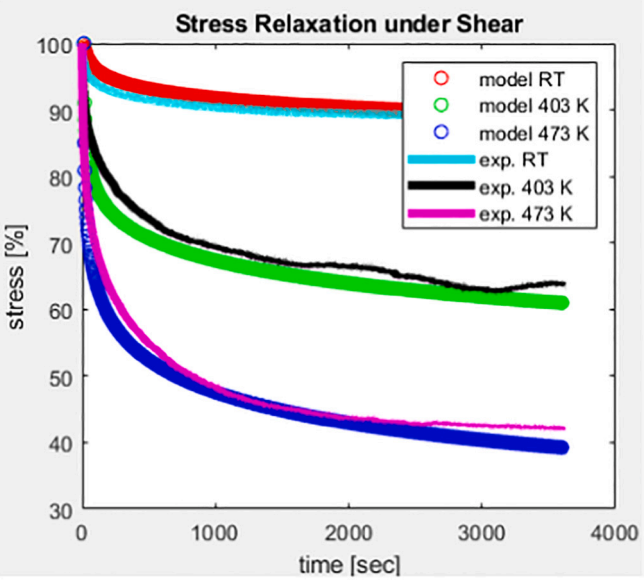

Fig. 4. Shear stress relaxation curves of the model compared to experimental results.

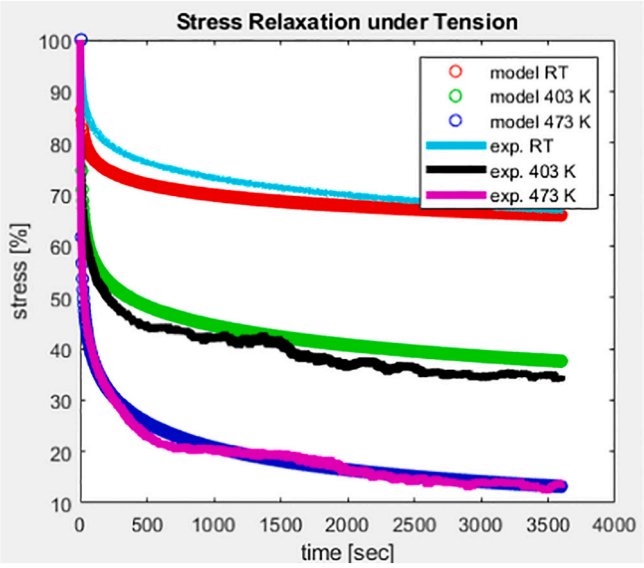

Fig. 5. Stress relaxation curves after tensile loading. Model calculations were fitted to experimental results.

For the case of cyclic loading under steady-state conditions, we here suggest a modified Coffin Manson lifetime model, where the number N_f of loading cycles to failure is expressed as

$$N_f = a\left(\frac{\Delta\varepsilon_{ine}}{\varepsilon^{mean}_f}\right)^b, \tag{15}$$

where a and b are material parameters, $\Delta\varepsilon_{ine}$ is the inelastic strain increment per loading cycle, and ε^{mean}_f is defined as

$$\varepsilon^{mean}_f = h_1 \bullet \exp\left\{-h_2 \bullet p^{mean}_{eff}\right\} \tag{16}$$

Here, p^{mean}_{eff} is the mean value of effective hydrostatic pressure, which is averaged over one period of cyclic deformation. Owing to a temperature dependence of ductility, the parameters a, b, h_1 and h_2 are

Table 2
Material parameters used for the plots of Figs. 4 and 5.

Temperature	Shear modulus	Bulk modulus
298 [K]	8460 [MPa]	18,333 [MPa]
403 [K]	7920 [MPa]	17,167 [MPa]
473 [K]	7580 [MPa]	16,417 [MPa]

Isotropic hardening	D_1	D_2	ε_0
Parameter	16 [MPa]	3	0.09

Kinematic hardening	k_1	k_2
Parameter	20 [MPa]	7

Activation energy	Threshold stress value A	Initial porosity
133 kJ/ (mol K) P	2.0 [MPa]	0.38

Creep	c_1	c_2	c_3
Coefficients	3e11	2e9	0.22

Stress	n_1 (volumetric)	n_2 (deviatoric)
Exponents	1.9	3.5

considered as temperature dependent.

3.4. Numerical fitting of material parameters

The material parameters of the model are determined from fits to mechanical tests under tension and shear loads.

The numerical fits shown in Figs. 4 and 5 were based on the assumption that the sintered material is homogeneously deformed so that conditions of uniaxial tension and simple shear are fulfilled to a good approximation. The fitting procedure was at first performed for shear tests, because this state of stress is purely deviatoric, and therefore the number of relevant fit parameters is reduced from the beginning. Thereafter, the remaining parameters were determined from fits to tests under tensile load.

Fig. 4 shows fits to stress relaxation experiments performed with lap-joints in shear mode at temperatures of RT, 403 K and 473 K. The initial shear stresses of these experiments were 30 MPa, 30 MPa and 23 MPa, respectively. Thus, fits at equivalent temperatures were performed for stress relaxation of dumbbell shaped samples after tensile loading, as depicted in Fig. 5. The initial tensile stresses of these experiments were 43.2 MPa, 30.7 MPa and 31.7 MPa respectively. The parameters determined through the fits of Figs. 4 and 5 are summarized in Table 2. The values of elastic material constants were chosen in agreement with literature data [17] for sintered silver of the same porosity.

4. FEM implementation in ABAQUS

The constitutive equations for the evolution of stresses, strains and porosity are now implemented in the commercial software ABAQUS Standard through user subroutine UMAT and in ABAQUS Explicit through user subroutine VUMAT [18], respectively. The implementation in ABAQUS Explicit is straightforward, but when applied to long time scales it gets computationally expensive. On the other hand, the implementation in ABAQUS Standard is more difficult to achieve, because the stiffness matrix of a nonlinear material has to be calculated. However, with use of this algorithm larger time increments can be evaluated, and therefore the computation is faster.

For simplicity, we here start with the algorithm used for the subroutine VUMAT: This subroutine is called for every increment of the simulation. The interface of the user subroutine to the main program is defined in the sense that stresses and state variables, which are valid at the beginning of the increment, are passed in by the main program together with incremental values dt for time and $\Delta\varepsilon$ for strain, respectively. The subroutine has to return the updated values for the stress tensor and the state variables at the end of the increment. The 8 state variables used in this algorithm are the components of the backstress tensor, the value of accumulated inelastic strain and the updated value for the porosity of the material.

In the first step of the algorithm, a trial stress

$$\sigma_{trial} = \sigma_{ini} + C \bullet (\varepsilon_{\mathrm{fin}} - \varepsilon_{\mathrm{ini}}) \tag{17}$$

is calculated, where C represents the elastic tensor. Further, the mean stress

$$\sigma_{mean} = \frac{1}{2}(\sigma_{ini} + \sigma_{trial}) \tag{18}$$

representing the time average of stress active in this increment is calculated. Next, the effective mean stress

$$\sigma^{eff}_{mean} = \sigma_{mean} - \chi_{ini} \tag{19}$$

is evaluated by subtraction of the backstress. Here, the backstress χ_{ini} for the beginning of the increment is inserted. Thus, the effective mean stress is decomposed into hydrostatic and deviatoric parts, and the correlated Euklidean norms of these tensors are calculated. Then, it is checked whether the inequality of Eq. (11c) is satisfied. In the case that the effective stresses are below the threshold value for creep, σ_{trial} is used as result for the stress at the end of the increment. Otherwise, the values for the volumetric and deviatoric strain rates are calculated according to Eqs. (11a) and (11b). In fact, the time increments used by ABAQUS Explicit are extremely small. Therefore, strains may be interpolated linearly within the increment, and one receives.

$$\Delta\varepsilon^{ine}_{vol} = \dot{\varepsilon}^{ine}_{vol} \bullet \mathrm{dt} \tag{20a}$$

and

$$\Delta\varepsilon^{ine}_{dev} = \dot{\varepsilon}^{ine}_{dev} \bullet \mathrm{dt}. \tag{20b}$$

Consequently, the stress at the end of the increment becomes

$$\sigma_{fin} = \sigma_{trial} - 2G\Delta\varepsilon^{ine}_{dev} - K\Delta\varepsilon^{ine}_{vol}, \tag{21}$$

where G and K are shear modulus and bulk modulus of an isotropic elastic material, respectively. Finally, the state variables are updated according to the equations

$$\chi_{\mathrm{fin}} = \chi_{ini} + k_1 \bullet \Delta\varepsilon_{\mathrm{ine}} - \mathrm{k}_2 \bullet \|\Delta\varepsilon_{\mathrm{ine}}\| \bullet \chi_{\mathrm{ini}} \tag{22}$$

$$\varepsilon^{ine}_{acc,fin} = \varepsilon^{ine}_{acc,ini} + \|\Delta\varepsilon_{ine}\| \tag{23}$$

$$f_{fin} = f_{ini} + (1 - f_{ini}) \bullet \Delta\mathrm{tr}(\varepsilon_{\mathrm{ine}}) \tag{24}$$

This update of the state variables completes the subroutine VUMAT.

Next, the subroutine UMAT for ABAQUS Standard is explained: The algorithm used for UMAT divides the time increment dt into N intervals, whereby every interval is evaluated according to the algorithm, which was already described in Eqs. (17) to (24). Thereby, N serves as solution parameter, and a value of $N = 10$ intervals proved to be useful. Further, the stresses and state variables at the end of every interval are used as start values for the subsequent interval. In consequence, one finally obtains the update for the stresses and state variables at the end of the time increment.

Furthermore, the 36 components of the material Jacobian matrix $\frac{\partial\Delta\sigma_{ij}}{\partial\Delta\varepsilon_{kl}}$ at the end of the increment are to be evaluated. This is done numerically with use of the stress update algorithm in combination with an increased strain increment $\Delta\varepsilon = \varepsilon_{fin} - \varepsilon_{ini}$. This procedure is carried out for every component of the strain tensor, whereby an additional strain increase of at least 10^{-12} per strain component was assumed.

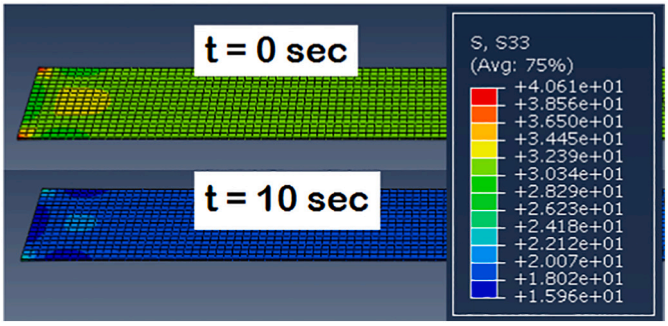

Fig. 6. Plot of tensile stress [MPa] for two time steps at 403 K. The stress relaxation within the first 10 s at constant sample length is shown.

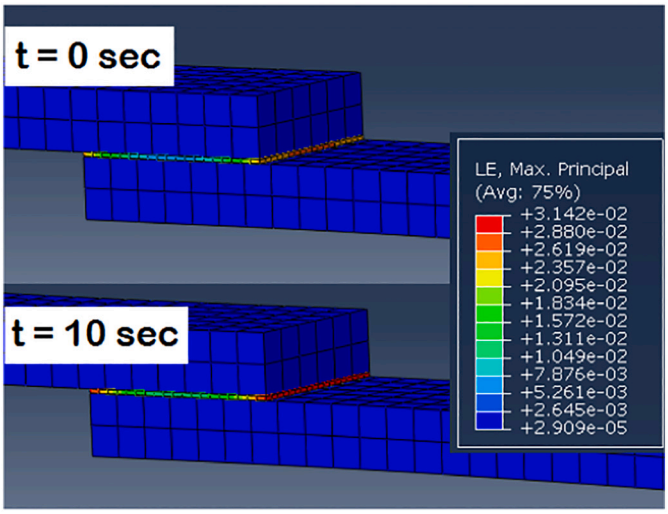

Fig. 7. Plot of first principal logarithmic strain for two time steps during stress relaxation at room temperature. An increase of inelastic strain within the sintered material is observed.

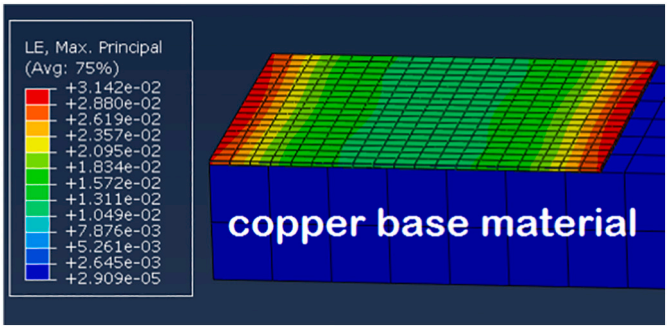

Fig. 8. Distribution of first principal logarithmic strain in the sintered material after 10 s of stress relaxation.

5. Simulation results

Examples of FEM simulations performed with subroutine UMAT are shown in Figs. 6–8. Fig. 6 shows the stress relaxation of a tensile specimen at 403 K using the material parameters of Table 2. For simplicity, only the parallel length of the sample was simulated. Prior to relaxation, the sample was loaded to 30.7 MPa within 8 s. Thereupon, the sample was kept at constant length. In Fig. 6, $t = 0$ indicates the time step of maximum stress at the onset of stress relaxation. 10 s later, a considerable stress reduction is observed. The material behaviour seen in the FEM simulation is in good agreement with the numerical results of Fig. 5, which was derived for a homogeneously deformed sample.

In Fig. 7 one can see the stress relaxation of a lap-joint at room temperature. The entire sample including the copper parts of 50 mm length was simulated. The Figure shows the region in the vicinity of the sintered area. The time step of t = 0 indicates the onset of stress relaxation after loading. Thereupon, further increase of inelastic strain is observed in the sintered material.

The cut view depicted in Fig. 8 shows the strain distribution in the sintered silver after 10 s of stress relaxation at room temperature.

Obviously, the distribution of strain is not homogeneous. Nevertheless, the amount of tensile stress reduction at the ends of the lap-joint appeared to be plausible with respect to experimental data. In conclusion, the material parameters of Table 2 can be used for modelling of sintered silver without need of further optimization.

6. Summary and conclusions

In summary, a unified material model for sintered silver was developed, which can be applied to reliability assessments of sintered joints in electronic packages. Lifetime estimates are usually deduced from models of damage accumulation, whereby damage develops in dependence of the accumulated inelastic strain observed during simulation of electronic assemblies [16]. In praxis, simplified material models as for instance bilinear kinematic hardening are used for this purpose. In this context, advanced material models for the sintered joints may provide more accurate estimates for expected lifetimes of electronic modules. However, follow up studies seem to be necessary in order to obtain further insight into damage accumulation. In particular, it is planned to study ageing effects of the sintered material in future investigations.

Declaration of competing interest

We have no conflict of interest regarding the manuscript submission: “Constitutive equations for strain rate and temperature dependent mechanical behaviour of porous Ag-sintered joints in electronic packages” for publication in Microelectronics Reliability, special issue of the ESREF conference!

Acknowledgements

The financial support by the Austrian Federal Ministry for Digital and Economic Affairs and the National Foundation for Research, Technology and Development is gratefully acknowledged.

References

[1] Jan A. Oestreicher, T. Röhrich, J. Wilden, M. Lerch, A. Jakob, H. Lang, An innovative method for joining materials at low temperature using silver (nano) particles derived from [AgO2C(CH2OCH2)3H], Appl. Surf. Sci. 265 (15) (2013) 239–244.
[2] Ch. Neeb, L. Böttcher, M. Conrad, R. de Doncker, nnovative and reliable power modules, IEEE Ind. Electron. Mag. (2014) 6–16. Sept.
[3] L. Boettcher, S. Karaszkiewicz, D. Manessis, A. Ostmann, Embedded die packages and modules for power electronics applications, IMAPS 2016 (2016) 001918–001947.
[4] Z. Gökdeniz, G. Khatibi, J. Nicolics, A. Steiger-Thirsfeld, Behaviour of silver-sintered joints by cycling mechanical loading and influence of temperature, in: IEEE Proc. of 22nd EMPC, 2019.
[5] Z. Gökdeniz, G. Khatibi, T. Walter, J. Nicolics, in: 41st International Spring Seminar on Electronics Technology (ISSE), 2018.
[6] Yu. Dun-ji, Xu. Chen, Gang Chen, Lu. Guo-quan, Zheng-qiang Wang, Applying Anand model to low-temperature sintered nanoscale silver paste chip attachment, Mater. Des. 30 (2009) 4574–4579.
[7] L. Anand, Constitutive equations for hot working of metals, Int J. Plasticity 1 (1985) 213–231.
[8] Gang Chen, Ze-Sheng Zhang, Yun-Hui Mei, Xin Li, Dun-Ji Yu, Lei Wang, Xu Chen, Applying viscoplastic constitutive models to predict ratcheting, Mech. Mater. 72 (2014) 61–71.
[9] Yao Yao, He Gong, Damage and viscoplastic behavior of sintered nano-silver joints under shear loading, Eng. Fract. Mech. 222 (2019) 106741.
[10] A.L. Gurson, J. Eng. Mater. Technol. 99 (1977) 2–15.

[11] J.L. Chaboche, A review of some plasticity and viscoplasticity constitutive theories, Int. J. Plast. 24 (2008) 1642–1693.
[12] Y. Kariya, H. Yamaguchi, M. Itako, N. Mizumura, K. Sasaki, J. Smart Process. 2 (2013) 160.
[13] F.A. McClintock, A criterion for ductile fracture by growth of holes, Am. Soc. Mech. Eng. 35 (1968) 363–371.
[14] J.R. Rice, D.M. Tracey, On the ductile enlargement of voids in triaxial stress fields, J. Mech. Phys. Solids 17 (1969) 201–217.
[15] G.R. Johnson, W.H. Cook, Fracture characteristics of three metals subjected to various strains, strain rates, temperatures and pressures, Eng. Fract. Mech. 21 (1) (1985) 31–48.
[16] P. Rajaguru, H. Lu, C. Bailey, Sintered silver finite element modelling and reliability based design optimisation in power electronic module, Microelectron. Reliab. 55 (2015) 919–930.
[17] J. Carr, X. Milhet, P. Gadaudb, S.A.E. Boyer, G.E. Thompson, P. Lee, Quantitative characterization of porosity and determination of elastic modulus for sintered micro-silver joints, J. Mater. Process. Technol. 225 (2015) 19–23.
[18] ABAQUS User Subroutine Manual Dassault Systemes.